

Microstrain in hydroxyapatite carbon nanotube composites

Catherine Kealley,^{a,b*} Margaret Elcombe^a and Arie van Riessen^c

^aBragg Institute, Australian Nuclear Science and Technology Organisation (ANSTO), PMB 1, Menai, NSW 2234, Australia, ^bDepartment of Chemistry, Materials and Forensic Science, University of Technology, Sydney, PO Box 123, Broadway, NSW 2007, Australia, and ^cCentre for Materials Research, Curtin University of Technology, GPO Box U1987, Perth, WA 684, Australia.
E-mail: catherine.kealley@ansto.gov.au

Synchrotron radiation diffraction data were collected from hydroxyapatite-carbon nanotube bioceramic composites to determine the crystallite size and to measure changes in non-uniform strain. Estimates of crystallite size and strain were determined by line-profile fitting of discrete peaks and these were compared with a Rietveld whole-pattern analysis. Overall the two analysis methods produced very similar numbers. In the commercial hydroxyapatite material, one reflection in particular, (0 2 3), has higher crystallite size and lower strain values in comparison with laboratory-synthesized material. This could indicate preferential crystal growth in the [0 2 3] direction in the commercial material. From the measured strains in the pure material and the composite, there was a degree of bonding between the matrix and strengthening fibres. However, increasing the amount of carbon nanotubes in the composite has increased the strain in the material, which is undesirable for biomedical implant applications.

© 2008 International Union of Crystallography
Printed in Singapore – all rights reserved

Keywords: strain; crystallite size; hydroxyapatite; nanotube; composite.

1. Introduction

Artificial hip joints and other surgical implants make severe demands on the material from which they are made. Given the ageing population and the inevitable need for biomedical implants, there is increasing demand on the biomaterials field for solutions that will improve mechanical properties, including strength and flexibility. Human bone is mainly composed of collagen and hydroxyapatite (HAp) nanocrystals. HAp has been produced synthetically, with a structure and chemical composition almost identical to the human bone. When implanted, these synthetic porous materials are accepted by the body. However, they have poor mechanical properties, making them unreliable for implant applications (Jarcho *et al.*, 1976).

The aim of this research was to combine biocompatible HAp with another biocompatible compound [carbon nanotubes (CNTs)] to form a composite material with improved physical properties. Multi-wall CNTs were used to reinforce the hydroxyapatite as they have exceptional mechanical properties, including extreme flexibility and strength, significant resistance to bending, high resilience and the ability to reverse any buckling of the tube (Bernholc *et al.*, 2000).

Synchrotron X-ray sources have a combination of high brightness and vertical collimation, resulting in diffractometers that are capable of producing very high resolution

patterns. Hence, synchrotron radiation diffraction (SRD) has the potential to provide considerably lower impurity phase detection limits owing to significant improvements in peak-to-background values relative to laboratory X-ray diffraction. Also the superior resolution offered by SRD gives improved estimates of microstrain and crystallite size. Line-profile fitting on discrete peaks as well as whole-pattern analysis is used to obtain estimates of crystallite size and strain. Measurement of differences in strain in HAp with and without CNTs provides direct evidence of the bonding between the matrix and strengthening fibres. It also assists in determining whether the increasing amount of CNTs in the material has a detrimental effect on the strain, which would be undesirable in terms of biomedical implant applications.

2. Methodology

The CNT material was supplied by MER Corporation, as a mixture of graphite, multi-wall CNTs (30–40 wt%) and soot. All other chemicals were AR grade and were supplied by the Sigma-Aldrich Chemical Company. The production method for the synthesized HAp was adapted from Jarcho *et al.* (1976). A 250 ml solution of 1.0 mol L⁻¹ Ca(NO₃)₂ was diluted to 500 ml with Milli-q water and brought to a pH of >11 with ~10 ml of concentrated NH₄OH. A 250 ml solution of

0.6 mol L⁻¹ (NH₄)₂HPO₄ was diluted again to 500 ml and then lifted to a pH of >11 with ~300 ml of concentrated NH₄OH. The dilutions were required to dissolve all of the reactants. The phosphate solution was added dropwise into the calcium solution, forming a white gelatinous precipitate. The precipitate was centrifuged, washed and oven dried at 383 K for 24 h. Optimization of this process has already been described (Kealley *et al.*, 2006).

Two production methods of incorporating CNTs into the HAp have been investigated: chemical precipitation reinforcement and physical reinforcement. For the chemical reinforcement, 5% by weight of CNT material (2% CNTs) was incorporated during the precipitation of the HAp. The CNT material was dispersed in the Ca(NO₃)₂ reactant before precipitation occurred. For the physical reinforcement, 5% by weight of CNT material was physically mixed with dried HAp powder for 30 min in a gyroscopic tumbler. A second set of samples were processed using a commercial HAp powder from Merck Pty Ltd. The dried commercial HAp powder and increasing amounts (5.0% C, 12.5% C and 25.0% C by weight) of CNT material were physically mixed for 30 min with a gyroscopic tumbler (Table 1 includes the complete list of samples).

Green bodies of the powders were produced by uniaxially pressing at 100 MPa, followed by cold isostatically pressing at 200 MPa. The compacts were then loaded into a steel can, which was lined with grafoil (rolled sheet of carbon graphite) to prevent the steel interacting with the sample. The cans were evacuated at 923 K before being hot isostatically pressed (HIP) at a pressure of 100 MPa at 1173 K for 2 h in an argon environment.

Sample discs with a thickness of ~1.2 mm were then sliced from the sintered material. For the synchrotron measurements, the sample discs were loaded directly into the sample holder. This holder was then placed into a custom-built sample stage which allowed rotation of the sample during data collection (see Fig. 1). Timing was such that more than one revolution was achieved per data step. Data from all samples were collected in reflection geometry on the 1-BM beamline at the Advanced Photon Source in Chicago, USA, with a wavelength of 0.061958 ± 0.000001 nm, a step size of 0.0015°, and an angle range from 8.65 to 46° 2θ.

2.1. Rietveld whole-pattern analysis

The Voigt function is the result of an analytical convolution of a Gaussian and a Lorentzian. Rietveld whole-pattern analysis was carried out using the program *Rietica* (Hunter *et al.*, 1995), which uses the Voigt profile function shown in (1),

$$G_{ik} = \frac{C_1^{1/2}}{H_{Gk}\pi^{1/2}} \operatorname{Re} \left[\omega \left(C_1^{1/2} X_{ik} + iC_3 \frac{H_{Lk}}{H_{Gk}} \right) \right], \quad (1)$$

Table 1

Selected parameters from Rietveld modelling (with a Voigt line profile) of the synchrotron diffraction data from physically mixed HAp and CNTs (values in parentheses correspond to the uncertainty in the least significant figure to the left).

Sample	Goodness of fit	Bragg factor	Crystallite size (nm)	Strain (%)
1 Synthesized pure HAp	7.94	3.67	87.2 (4)	0.07 (1)
2 Synthesized HAp–5% C	8.46	3.82	92.8 (5)	0.06 (1)
3 Synthesized HAp–5% C	5.35	5.14	208 (1)	0.045 (5)
Impurity phase		4.58	750 (10)	0.041 (5)
4 Commercial pure HAp	15.95	5.61	1000 (10)	0.025 (2)
5 Commercial HAp–5% C	15.87	5.80	1460 (20)	0.025 (2)
6 Commercial HAp–12% C	9.36	4.07	521 (3)	0.027 (3)
7 Commercial HAp–25% C	9.45	5.25	463 (3)	0.032 (3)

where $C_1 = 2\ln 2$, $C_3 = 0.5\ln 2$, H_{Gk} is the full width at half-maximum (FWHM) of the contributing Gaussian, H_{Lk} is the FWHM of the contributing Lorentzian, ω is the complex error function [$\omega(z) = \exp(z^2)\operatorname{erfc}(z)$] (Langford, 1978, p.11), and Re denotes its real part.

In the case of the Voigt profile function, the Gaussian width component H_{Gk} varies in accordance with equation (2). The Lorentzian width component H_{Lk} varies in accordance with equation (3), which is based on the Scherrer equation,

$$H_{Gk} = (U \tan^2 \theta + V \tan \theta + W)^{1/2}, \quad (2)$$

$$H_{Lk} = (180/\pi)(\lambda/D) \sec \theta = K_s \sec \theta, \quad (3)$$

where λ is the wavelength, D is the crystallite size parameter, U , V and W are the peak profile parameters, and K_s is the Lorentzian parameter ‘size – γ_0 ’ from the refinement model.

Strain values were extracted from the Gaussian component [equation (2)] of the refined values as follows. A model of the data collected from the LaB₆ standard material (NIST standard 660a) was refined, and the peak profile parameters U , V and W obtained. For all sample refinements, parameters V and W were fixed at these values representing the instrumental broadening. The instrumental contribution to the strain, U_{inst} ,

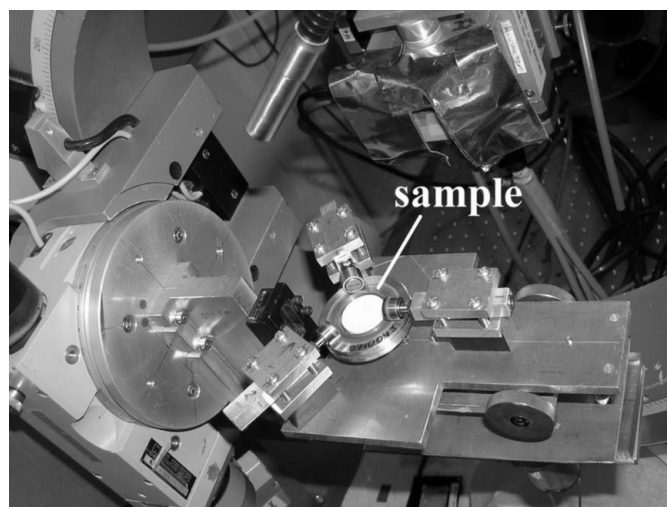


Figure 1 Custom-designed sample holder and spinner mounted in station C on 1-BM at the Advanced Photon Source. The diameter of the sample is ~20 mm.

was subtracted from the refined U_{obs} parameters for the respective samples. The root-mean-square strain $\langle \varepsilon^2 \rangle^{1/2}$ was calculated using equation (4) (van Riessen, 1987), and the result multiplied by 100 to obtain the strain (%),

$$\langle \varepsilon^2 \rangle = \frac{\pi^2(U_{\text{obs}} - U_{\text{inst}})}{720^2 (2 \ln 2)}. \quad (4)$$

Using the Lorentzian width component [equation (3)], the crystallite size was determined from the simplified formula in equation (5),

$$D = (180/\pi)(\lambda/K_s), \quad (5)$$

where K_s incorporates the Lorentzian component as a function of the observed size, γ_{obs} , and the instrumental contribution, γ_{inst} . For this work the instrumental contribution was also determined from the refinement of a model from the LaB₆ standard material, which was used to accurately calibrate wavelength and characterize the beam profile.

The crystallographic models used for Rietveld refinement were a hexagonal hydroxyapatite phase [Ca₁₀(PO₄)₆(OH)₂] and a rhombohedral β -calcium phosphate phase [β -Ca₃(PO₄)₂]. The Ca₁₀(PO₄)₆(OH)₂ phase has a *P63/m* space group, with $a = b = 0.94166$ nm, $c = 0.68745$ nm, $\alpha = \beta = 90^\circ$ and $\gamma = 120^\circ$ (Hughes *et al.*, 1989). The β -Ca₃(PO₄)₂ phase has the mineral name whitlockite, space group *R3cH*, with $a = b = 1.0439$ nm, $c = 3.7375$ nm, $\alpha = \beta = 90^\circ$ and $\gamma = 120^\circ$ (Dickens *et al.*, 1974).

2.2. Discrete-peak analysis

One drawback of a whole-pattern refinement like the Rietveld analysis is that all of the peaks are fitted with the same peak profile function (U , V , W). This makes it difficult to determine (or quantify) if there is any anisotropy present. Discrete peak-profile analysis allows the crystallite size and strain to be calculated for individual reflections. If a specific set of reflections is broader or narrower than the rest, it may mean that a specific set of planes are under strain, or there has been preferential crystallite growth in one direction. Crystallite size and non-uniform strain information can be calculated by discrete-peak-profile analysis using the method proposed by de Keijser *et al.* (1982). It has been experimentally verified (de Keijser *et al.*, 1983) that crystallite-size broadening can be approximated by the Lorentzian (Cauchy) function shown in equation (6),

$$L^v(x) = \left(1 + \frac{\pi^2 x^2}{\beta_L^2}\right)^{-1} = \left[1 + \frac{4x^2}{(\text{FWHM}_L)^2}\right]^{-1}. \quad (6)$$

Strain broadening can be described by the Gaussian function in equation (7),

$$G^v(x) = \exp\left(\frac{-\pi x^2}{\beta_G^2}\right) = \exp\left[\frac{-(4 \ln 2)x^2}{(\text{FWHM}_G)^2}\right], \quad (7)$$

where L^v and G^v denote the Lorentzian and Gaussian functions with integral breadths β_L and β_G , and full width at half-maximums FWHM_L and FWHM_G , respectively. A convolution of the Lorentzian and Gaussian functions is discussed by

Langford (1978) and it is known as the Voigt function. The program *SigmaPlot* (Systat Software Inc., 2004) was used to separately fit the Lorentzian and Gaussian functions to the selected discrete peaks. Once fitted, the FWHM was used to calculate the Lorentzian integral breadth β_L and the Gaussian integral breadth β_G for each selected peak. The integral breadths were then inserted into equations (8) and (9) (de Keijser *et al.*, 1982) to calculate the crystallite size and strain values for each selected peak,

$$\text{size (nm)} = \frac{\lambda}{(\beta_L - \beta_{L1}) \cos \theta}, \quad (8)$$

$$\text{strain (\%)} = 100 \frac{(\beta_G^2 - \beta_{G1}^2)^{1/2}}{4 \tan \theta}. \quad (9)$$

Here, λ is the wavelength, θ is the angular position of the peak, and β_{L1} and β_{G1} are the instrument function breadths calculated from the LaB₆ data.

3. Results

All synchrotron data collected have been analysed using *Rietica* (Hunter *et al.*, 1995). It should be noted that an impurity phase (shown in Fig. 2), β -Ca₃(PO₄)₂, was identified in the HAp + 5% C physically mixed sample. The OH functional group has been removed from the HAp matrix (dehydration), resulting in the decomposition of the HAp phase. The decomposition of HAp is accompanied by a decrease in mechanical properties owing to a reduction in densification (Jarcho *et al.*, 1976) and this is undesirable for biomedical implant applications.

The crystallite size and strain have been determined from a Rietveld refinement of the whole pattern for each of the seven samples. These values, as well as the goodness-of-fit and the Bragg factor, are listed in Table 1. The goodness-of-fit is determined by a comparison of the entire observed pattern

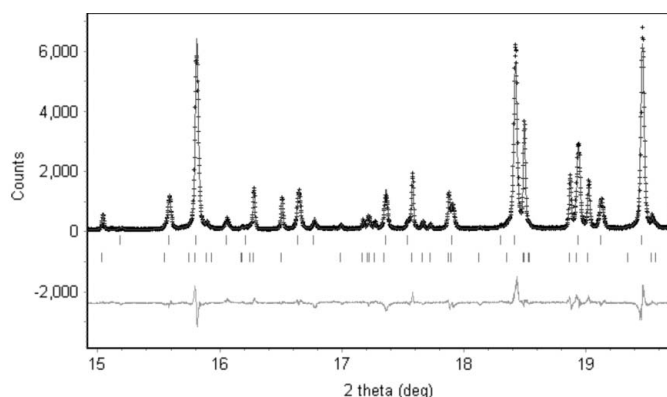


Figure 2 Rietveld refinement of the models of the SRD data collected from the synthesized HAp-5% C mixed sample for a selected 2θ range. The observed plot is the crosses, the calculated plot is the continuous line through the observed data, the upper set of vertical lines underneath the plot represent the peak position markers for a hexagonal hydroxyapatite phase [Ca₁₀(PO₄)₆(OH)₂], the lower set of vertical lines are for the rhombohedral β -calcium phosphate phase [β -Ca₃(PO₄)₂], and the difference plot is below the peak markers.

with the entire calculated pattern (Young, 1993). If there are observed intensities (for example, an impurity phase) that are not accounted for with the calculated model, then the goodness-of-fit will be large, indicating a poor fit. The Bragg factor is based on structural modelling of calculated intensities, and does not include intensities observed at other locations. This means that the Bragg factor only includes peaks aligned with the phase(s) being modelled; it does not incorporate any 'misfits' in the pattern (Young, 1993). All of the Bragg factors listed in Table 1 were deemed acceptable (<10). Hence the U_{obs} and γ_{obs} parameters determined from the modelled Bragg intensities were suitable for crystallite size and strain calculations for the respective phases, even though the actual goodness-of-fit for some of the refinements was poor.

Synchrotron X-rays have a combination of high brightness and vertical collimation, resulting in diffractometers with very high resolution. This resolution reduces the problems found with peak overlaps, and hence allowed four relatively high intensity reflections that were free from overlap to be selected for discrete-peak analysis for the HAp samples. It should also be mentioned that reflections with lower intensities had to be used for the synthesized HAp + 5% C physically mixed sample with the impurity phase, as the impurity phase overlapped a lot of the pure HAp reflections. The errors are correspondingly larger. The crystallite size and strain for four discrete peaks in each sample are given in Table 2.

4. Discussion

It can be seen from Table 1 that the crystallites in the commercial pure HAp are more than ten times the size of the synthesized pure HAp (precursor powders have a similar crystal size), and have less than half of the strain. This lower strain could be a result of the relatively unconstrained growth of the crystallites during the HIP process, while the crystallites in the laboratory-synthesized samples have been pinned with a concomitant higher level of strain. As can be seen in Table 1, the addition of the CNT material to the synthesized HAp during precipitation resulted in minimal change in crystallite size or strain. Physical mixing of 5% of the CNT material with the commercial HAp has resulted in an increase in crystallite size relative to the commercial pure HAp. However, sintered commercial HAp samples with 12% and 25% CNT material show significantly lower crystallite size (approximately half of the original crystallite size of the commercial HAp pure HIP sample). Inclusion of increasing amounts of CNT material has had no effect (within experimental error) on the strain in the samples, which suggests there is little or no bonding between the two materials. It should be noted that the inclusion of the CNT material shows an improvement in the goodness-of-fit parameters listed in Table 1, as the slightly higher background due to the carbon material has masked the majority of the impurity peaks.

Both Tables 1 and 2 show that the difference between the addition of the carbon nanotube material during precipitation resulted in no significant change, and the formation of an impurity phase in the synthetic HAp–5% C physically mixed

Table 2

Crystallite size and strain calculated from the integral line breadths of four discrete peaks of the synchrotron data, from each of the seven samples (values in parentheses correspond to the uncertainty in the least significant figure to the left).

Sample	Reflection (<i>h k l</i>)	Crystallite size (nm)	Strain (%)	
1 Synthesized pure HAp	0 2 3	93 (3)	0.079 (4)	
	1 2 3	94 (2)	0.078 (3)	
	2 3 1	83 (2)	0.080 (2)	
2 Synthesized HAp–5% C Precipitated	1 4 0	80 (2)	0.080 (2)	
	0 2 3	107 (3)	0.074 (4)	
	1 2 3	104 (2)	0.071 (2)	
	2 3 1	88 (2)	0.078 (2)	
3 Synthesized HAp–5% C Physically mixed	1 4 0	85 (2)	0.078 (2)	
	2 3 0	174 (7)	0.045 (2)	
	1 3 3	192 (8)	0.035 (3)	
	3 3 0	130 (10)	0.04 (1)	
	2 4 0	159 (5)	0.040 (2)	
	Whitlockite	1 1 12	690 (60)	0.032 (6)
	Impurity phase	1 3 1	710 (80)	0.033 (5)
4 Commercial pure HAp	0 3 12	460 (30)	0.031 (2)	
	3 3 0	370 (40)	0.030 (4)	
	0 2 3	1640 (260)	0.0209 (5)	
	1 2 3	1200 (100)	0.0197 (3)	
	2 3 1	1300 (100)	0.0195 (3)	
5 Commercial HAp–5% C	1 4 0	1150 (80)	0.0197 (3)	
	0 2 3	2300 (500)	0.0201 (3)	
	1 2 3	1640 (160)	0.0190 (2)	
	2 3 1	1530 (140)	0.0189 (2)	
6 Commercial HAp–12% C	1 4 0	1440 (120)	0.0188 (2)	
	0 2 3	720 (50)	0.0254 (8)	
	1 2 3	670 (30)	0.0236 (5)	
	2 3 1	660 (30)	0.0234 (5)	
7 Commercial HAp–25% C	1 4 0	600 (20)	0.0236 (5)	
	0 2 3	510 (30)	0.029 (1)	
	1 2 3	470 (10)	0.0270 (5)	
	2 3 1	450 (10)	0.0272 (5)	
	1 4 0	440 (10)	0.0271 (5)	

sample has resulted in an increase in the crystallite size of HAp phase after the HIP process. In terms of the commercial HAp material, the results in Table 2 show that the inclusion of 5% of the CNT material has resulted in an increase in crystallite size, while further addition of 12% and 25% CNT material results in significantly smaller crystallite sizes in the post-HIP material.

Overall the numbers determined from the discrete-peak analysis are in general agreement with those obtained from the full-pattern analysis. The largest difference between the two analysis methods is the noticeable increase in strain ($>40\%$) as the amount of CNT material is increased, when analysed as discrete peaks. This measurable increase in strain with increase in amount of added CNTs indicates that there is a degree of bonding between the CNTs and the matrix. The Rietveld refined data show the same trend, but it is not statistically significant. Table 2 shows that the discrete-peak analysis results for the four reflections chosen appear to be in agreement (within experimental error) for each of the samples and, hence, the strain is isotropic. However, one reflection in particular, (0 2 3), has higher crystallite size and strain values in the commercial material in comparison with the other three reflections. This peak is the weakest of the four fitted, and has the largest error. If further work shows this variation is real,

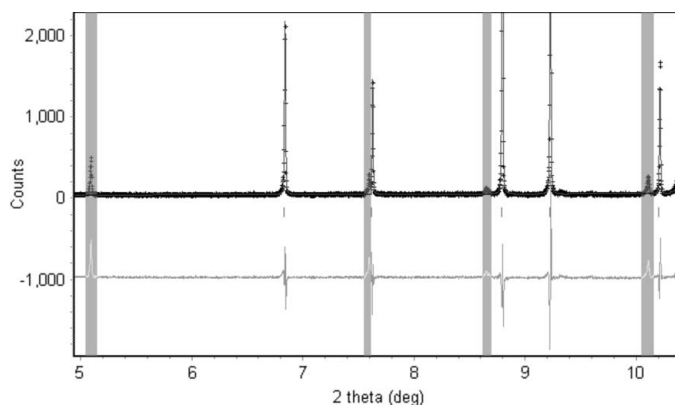


Figure 3
A selected 2θ region from the Rietveld refinement of the SRD data collected from commercial HAp material post-HIP. The shaded grey regions highlight an example of the small peaks that are unaccounted for by the HAp phase. The observed plot is the crosses, the calculated plot is the continuous line through the observed data, the vertical lines underneath the plot represent the peak position markers for a hexagonal hydroxyapatite phase, $[\text{Ca}_{10}(\text{PO}_4)_6(\text{OH})_2]$, and the difference plot is below the peak markers.

this could indicate preferential crystal growth in the $[0\ 2\ 3]$ direction in the commercial material. This trend is not present in the laboratory-synthesized samples.

The SRD data shown in Fig. 3 also identify that there are very weak unexplained diffraction peaks indicative of an impurity phase present in the commercial HAp material. The Bragg factor implies that the HAp phase has been accurately refined; however, there are other components in the material that have not been accounted for by the model. The label on the container quoted 90% HAp purity, with 5% H_2O , and small traces of Cl, F, SO_4 , Pb, Fe and As ions, leaving 4.4% unaccounted for. The peaks from the impurity phases in the starting material overlap with peaks from the expected phase(s) from the HIP, preventing identification. As a result, it has not been possible to refine these peaks, and hence they have been excluded from the whole-pattern analysis refinements.

5. Summary

A comparison of the results from the whole-pattern analysis and the discrete-peak analysis shows that there is general agreement in the values of strain and crystallite size. The

majority of the strain is isotropic; however, one reflection in particular, $(0\ 2\ 3)$, has higher crystallite size and strain values in the commercial material. This could indicate preferential crystal growth in the $[0\ 2\ 3]$ direction in the commercial material. The samples with the highest strain were the laboratory-synthesized materials, suggesting that there is a thermal contraction mismatch. The inclusion of increasing amounts of CNT material has a slight effect on the strain in the HAp, suggesting that there may be a small amount of bonding between the two materials.

CK was supported by a University of Technology, Sydney Doctoral Scholarship and a Post-graduate Research Award from the Australian Institute of Nuclear Science and Engineering. The synchrotron diffraction work was supported by the Australian Synchrotron Research Program, which is funded by the Commonwealth of Australia under the Major National Research Facilities Program. Use of the Advanced Photon Source was supported by the US Department of Energy, Office of Science, Basic Energy Sciences, under Contract No. W-31-109-Eng-38.

References

- Bernholc, J., Nardelli, M. B., Fattebert, J. L., Orlikowski, D., Roland, C. & Zhao, Q. (2000). *Science and Application of Nanotubes*, edited by D. Tomanek & R. J. Enbody, p. 195. New York: Kluwer Academic/Plenum.
- Dickens, B., Schroeder, L. W. & Brown, W. E. (1974). *J. Solid State Chem.* **10**, 232–248.
- Hughes, J. M., Cameron, M. & Crowley, K. D. (1989). *Am. Mineral.* **74**, 870–876.
- Hunter, B. A., Hill, R. J. & Howard, C. J. (1995). *Rietica. A computer program for Rietveld analysis of fixed-wavelength X-ray and neutron powder diffraction patterns*. ANSTO, Australia.
- Jarcho, M., Bolen, C. H., Thomas, M. B., Bobick, J., Kay, J. F. & Doremus, R. H. (1976). *J. Mater. Sci.* **11**, 2027–2035.
- Kealley, C., Ben-Nissan, B., van Riessen, A. & Elcombe, M. (2006). *Key Eng. Mater.* **309–311**, 597–600.
- Keijsers, Th. H. de, Mittemeijer, E. J. & Rozendaal, H. C. F. (1983). *J. Appl. Cryst.* **16**, 309–316.
- Keijsers, Th. H. de, Langford, J. I., Mittemeijer, E. J. & Vogels, A. B. P. (1982). *J. Appl. Cryst.* **15**, 308–314.
- Langford, J. I. (1978). *J. Appl. Cryst.* **11**, 10–14.
- Riessen, A. van (1987). PhD thesis. Curtin University of Technology, Australia.
- Systat Software Inc. (2004). *SigmaPlot*. Version 9.0. Richmond, CA, USA.
- Young, R. A. (1993). *The Rietveld Method*. Oxford University Press.